ADVANCED MATERIALS
www.advmat.de

Ultralow-Temperature Li/CF_x Batteries Enabled by Fast-Transport and Anion-Pairing Liquefied Gas Electrolytes

Yijie Yin, John Holoubek, Alex Liu, Baharak Sayahpour, Ganesh Raghavendran, Guorui Cai, Bing Han, Matthew Mayer, Noah B. Schorr, Timothy N. Lambert, Katharine L. Harrison, Weikang Li, Zheng Chen,* and Y. Shirley Meng**

Lithium fluorinated-carbon (Li/CF_x) is one of the most promising chemistries for high-energy-density primary energy-storage systems in applications where rechargeability is not required. Though Li/CF_x demonstrates high energy density (>2100 Wh kg^{-1}) under ambient conditions, achieving such a high energy density when exposed to subzero temperatures remains a challenge, particularly under high current density. Here, a liquefied gas electrolyte with an anion-pair solvation structure based on dimethyl ether with a low melting point (–141 °C) and low viscosity (0.12 mPa s, 20 °C), leading to high ionic conductivity (>3.5 mS cm^{-1}) between –70 and 60 °C is reported. Besides that, through systematic X-ray photoelectron spectroscopy integrated with transmission electron microscopy characterizations, the interface of CF_x is evaluated for low-temperature performance. The fast transport and anion-pairing solvation structure of the electrolyte are concluded to bring about reduced charge-transfer resistance at low temperatures, which results in significantly enhanced performance of Li/CF_x cells (1690 Wh kg^{-1}, –60 °C based on active materials). Utilizing 50 mg cm^{-2} loading electrodes, the Li/CF_x still displays 1530 Wh kg^{-1} at –60 °C. This work provides insights into the electrolyte design that may overcome the operational limits of batteries in extreme environments.

1. Introduction

Primary batteries serve an indispensable role in providing sustainable power in extreme environments which require long storage and operation life.[1] Thus, there is an escalating demand for primary batteries with high energy/power density and extreme-temperature adaptability.[2] Amongst the well-known primary batteries, Li/fluorinated-carbon (Li/CF_x) presents itself as one of the most promising candidates for satisfying the above requirements.[3] At the same time, other chemistries, for example, Li/manganese oxide (Li/MnO_2), Li/sulfur dioxide (Li/SO_2), and Li/thionyl chloride (Li/$SOCl_2$), suffer from swelling,[4] gas venting, and toxicity.[5,6] Li/CF_x is a lightweight, safe, and highly stable system with a low self-discharge rate of <0.5% per year at room temperature with the highest theoretical energy density up to 2180 Wh kg^{-1} (CF_1 based on active materials).[7] However, the Li/CF_x batteries suffer an inferior rate and low-temperature (low-*T*) performance due to the sluggish bulk electrolyte transport and increased charge-transfer impedance.[8,9] To overcome the above challenges, the kinetic limitations of Li/CF_x must be understood and addressed. These include: 1) Li^+ diffusion through the solid electrolyte interface (SEI) and cathode electrolyte interface (CEI) layers;[10] 2) Li^+ solvation and de-solvation processes; 3) Li^+ diffusion through bulk electrolytes; 4) Li^+ insertion

Y. Yin, Z. Chen, Y. S. Meng
Materials Science and Engineering Program
University of California
La Jolla, San Diego, CA 92093, USA
E-mail: zhengchen@eng.ucsd.edu; shirleymeng@uchicago.edu

J. Holoubek, A. Liu, B. Sayahpour, G. Raghavendran, G. Cai, B. Han, M. Mayer, W. Li, Z. Chen, Y. S. Meng
Department of Nano Engineering
University of California
La Jolla, San Diego, CA 92093, USA
E-mail: wel001@eng.ucsd.edu

N. B. Schorr
Department of Power Sources R&D
Sandia National Laboratories
Albuquerque, NM 87123, USA

The ORCID identification number(s) for the author(s) of this article can be found under https://doi.org/10.1002/adma.202207932.

DOI: 10.1002/adma.202207932

T. N. Lambert
Department of Photovoltaics and Materials Technology
Sandia National Laboratories
Albuquerque, NM 87123, USA

K. L. Harrison
Nanoscale Sciences Department
Sandia National Laboratories
Albuquerque, NM 87123, USA

Z. Chen, Y. S. Meng
Sustainable Power and Energy Center
University of California
La Jolla, San Diego, CA 92093, USA

Y. S. Meng
Pritzker School of Molecular Engineering
University of Chicago
Chicago, IL 60637, USA

and/or diffusion in CF–CF layers;[11] 5) C—F bond breaking. Of the steps above, 1–4 are directly related to the electrolyte, indicating that the electrolyte plays a major role in governing the low-*T* behavior. However, current electrolyte research prioritizes the pursuit of performance rather than a comprehensive understanding of the dominating factors governing low-*T* behavior.

Historically, electrolyte designs for low-temperature Li/CF_x batteries have prioritized low freezing points and low-viscosity solvents to optimize the Li^+ transport. Tracing back to the effective conventional electrolytes for low-*T* CF_x batteries, NASA's Jet Propulsion Laboratory first reported an electrolyte formula consisting of 1 M lithium tetrafluoroborate ($LiBF_4$) coupled with 4:1 dimethoxyethane (DME):propylene carbonate (PC), which could deliver more than 600 mAh g^{-1} capacity at C/40 rate under –40 °C.[12] The optimized salt concentration and tris(2,2,2-trifluoroethyl) borate (TTFEB) additive further enhanced the specific capacity to around 300 mAh g^{-1} at C/5 rate under –60 °C.[9] Additionally, the utilization of acetonitrile outperformed the DME system at both power capability (C/10) and low-temperature discharge performance (–60 °C).[13] This was due to its improved ionic conductivity (5 to 11 mS cm^{-1}), facilitating bulk electrolyte transport at low temperatures. However, recent reports detailing the insertion of solvated Li^+ into the CF_x lattice and the formation of a ternary intermediate C-(solvated Li^+-F) imply that the electrolyte solvation structure directly influences the charge-transfer resistance as well, which is known to be crucial at low-temperature.[11,14] To this end, replacing strongly solvating DME with relatively weak solvating methyl butyrate (MB), which enabled an anion-pairing solvation structure, has been shown to improve both the high rate and low-temperature performance of Li/CF_x cells. The authors demonstrated an improved rate performance (1 C, 834 mAh g^{-1}) and a 240 mAh g^{-1} discharge capacity under –70 °C at 0.5 V cutoff voltage, although the formulated electrolyte delivered less than 1 mS cm^{-1} ionic conductivity at –70 °C.[15] Therefore, the design criteria of low-*T* electrolytes for CF_x batteries are either fast bulk ionic transport, formulation of anion-pair solvation structures, or integration of both parameters, where more recent studies demonstrated the anion-pair solvation structure may predominate the low-*T* discharge kinetics.[16,17] However, the pursuit of both factors is mostly contradictory and rarely reported in the battery field. The formation of anion-pair structures requires the increase of salt concentration or the addition of inert diluents to form a locally high salt-to-solvent ratio, which reduces the ionic conductivity of the electrolyte and increases viscosity.[18,19] On the contrary, the dilute concentration electrolytes often offer higher ionic conductivities, but they may suffer from the sluggish de-solvation process due to stronger Li^+-solvent coordination at reduced temperatures especially when using solvents with high solvating power.[17,20] Apart from the above discussions, electrolytes also determine the properties of the anode/electrolyte interphase (SEI) and cathode/electrolyte interface (CEI). For example, SEI formed on lithium metal vary at different temperature and is proven to affect the low-*T* lithium-metal cycling efficiency.[21] Given the sensitivity of the CEI formed at CF_x and the significant volume expansion after CF_x discharge, there is no clear report on the chemical composition of the CEI at sub-zero temperature and its correlation with low-*T* performance.

Owing to the ultralow melting point and viscosity of gaseous molecules,[22] transformative liquefied gas electrolytes (LGE) based on hydrofluorocarbons (e.g., fluoromethane) were reported to deliver a superior electrochemical performance with Li/CF_x at –40 °C although it offers <1 mS cm^{-1} ionic conductivity.[23] When paired with co-solvents, the formulated LGE improves the salt solubility and enables an anion-pairing solvation structure while maintaining a rapid transport at reduced temperature.[24,25] These unique features of LGE strongly indicate a promising candidate for low-*T* Li/CF_x batteries.

Herein, we formulated a new LGE based on dimethyl ether (Me_2O) and PC, maintaining an ionic conductivity >3.5 mS cm^{-1} from –70 to 60 °C. Due to the weak solvating power of Me_2O, the formulated electrolyte enables improved rate and low-temperature performance. The Li/CF_x cell utilizing a 4.3 mg cm^{-2} loading CF_x cathode delivered 780 mAh g^{-1} (91% room-temperature capacity retention) under 10 mA g^{-1} at –60 °C. Moreover, when 50 mg cm^{-2} CF_x is utilized, the cell still displays 706 mAh g^{-1} (84% room-temperature capacity retention) at –60 °C and the average discharge voltage can be maintained above 2.1 V. Furthermore, a systematic study combining different advanced characterizations was conducted to figure out the improving mechanism, including both the bulk and interphase aspects.

2. Results

An ideal electrolyte for ultralow temperature and high-rate Li–CF_x primary batteries should offer the lowest possible melting point (<–100 °C) and low viscosity. Besides, the electrolyte should easily de-solvate from its solvation shell, which brings about reduced charge-transfer resistance.[14] The Me_2O shows an ultralow melting point of –141 °C and a viscosity of 0.12 mPa s at 20 °C, which outperforms DME with –58 °C and 0.46 mPa s, acetonitrile (ACN) with –45 °C and 0.343 mPa s, tetrahydrofuran (THF) with –108 °C and 0.456 mPa s, and the recently reported MB with –95 °C and 0.526 mPa s (**Figure 1**a). Among gaseous solvents, Me_2O endows higher salt solubility than fluoromethane (FM) and difluoromethane (DFM) owing to the higher Lewis basicity of the C—O—C than C—F,[26] further enhancing electrolyte's ionic conductivity. In addition, Me_2O has been proven to offer excellent lithium-metal compatibility at a wide temperature range.[27] Considering the above features, Me_2O is introduced to replace DME in the conventional $LiBF_4$-DME-PC formulations. We first optimized the ratio between Me_2O and PC to maximize transport properties and discharge performance. As shown in Figure S1, Supporting Information, when the volume ratio reaches 6.5:1, the optimized electrolyte delivered the highest ionic conductivity of 3.54 mS cm^{-1} at –70 °C and the highest room-temperature discharge capacity and nominal voltage. Furthermore, different lithium salts in 6.5:1 volume ratio of Me_2O:PC electrolytes have been evaluated, and we found $LiBF_4$ exhibited optimal CF_x capacity utilization and discharge overpotential over lithium bis(fluorosulfonyl) imide (LiFSI) and lithium bis(trifluoromethanesulfonyl)imide (LiTFSI) salts at room temperature (Figure S2, Supporting Information), which is in alignment with previously reported

a

Solvent	Melting Point (°C)	Boiling Point(°C)	Critical Point(°C)	Viscosity (mPa·s)
Dimethyl Ether	–141	–24	127	0.12
Propylene Carbonate	–48.8	242	377	2.5
Tetrahydrofuran	–108	66	268	0.456
Acetonitrile	–45	82	272	0.343
1,2- Dimethoxyethane	–58	85	263	0.46
γ-Butyrolactone	–43.5	204	436	1.7
Methyl butyrate	–95	102	281	0.526
Fluoromethane	–142	–78	44	0.085
Difluromethane	–136	-52	78	0.12

b

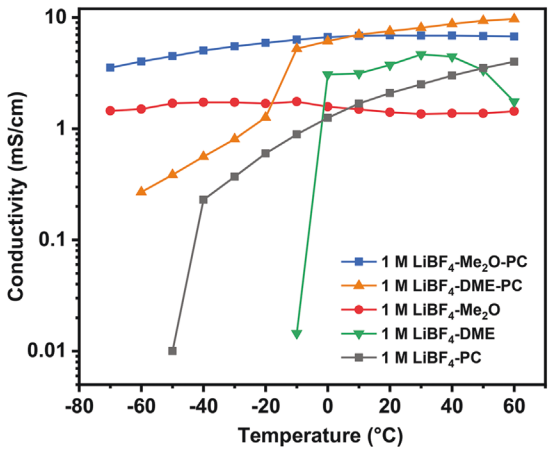

Figure 1. Design of the low-*T* electrolytes. a) Summary of physical properties of different solvents, data extracted from published works.[27,29] b) Measured ionic conductivities of the investigated electrolytes at different temperatures.

results that $LiBF_4$ could reduce the activation energy for the charge-transfer process.[28] Thus, the 1 M $LiBF_4$ in Me_2O:PC at a 6.5:1 volume ratio was formulated as the optimized electrolyte, hereby denoted as 1 M $LiBF_4$-Me_2O-PC. 1 M $LiBF_4$ in DME:PC with 6.5:1 volume ratio (denoted as 1 M $LiBF_4$-DME-PC), 1 M $LiBF_4$ in DME (denoted as 1 M $LiBF_4$-DME), and 1 M $LiBF_4$ in Me_2O (denoted as 1 M $LiBF_4$-Me_2O) are chosen as control systems for the mechanism study.

The ionic conductivities were measured to investigate the transport properties, as shown in Figure 1b. Owing to the superior physical properties of Me_2O, the 1 M $LiBF_4$-Me_2O-PC and 1 M $LiBF_4$-Me_2O demonstrated stable ionic conductivity from –70 to +60 °C. Among them, 1 M $LiBF_4$-Me_2O-PC invariably displayed > 3.5 mS cm^{-1}, higher than the electrolyte without PC. In contrast, although the conventional 1 M $LiBF_4$-DME-PC exhibited an ionic conductivity of > 4 mS cm^{-1} before –10 °C, a large drop was observed (< 1 mS cm^{-1}) below –20 °C, which is due to the salt precipitation from the electrolyte (Figure S3, Supporting Information). Similarly, severe ionic conductivity drops were observed for the other liquid 1 M $LiBF_4$-PC and 1 M $LiBF_4$-DME systems at reduced temperatures, mainly caused by the salt precipitation or the freezing of the electrolytes.

The solvation structure of the electrolyte influences the Li^+ de-solvation process,[16] as commonly depicted by Molecular dynamics (MD) simulation and Raman spectroscopy.[30] Here, both techniques were applied to understand the effect of solvent selection on anion-pairing. 1 M $LiBF_4$-Me_2O-PC, 1 M $LiBF_4$-DME-PC, 1 M $LiBF_4$-PC, and 1 M $LiBF_4$-Me_2O were directly compared with the individual solvents and salt. Based on the Raman spectra in **Figure 2**a, the solvated BF_4^- (B-F stretching) in the 1 M $LiBF_4$-Me_2O-PC exhibited a blueshift compared with the DME-PC counterpart, indicating more anions participate in the solvation shell.[31] As for the C—O—C stretching of Me_2O (Figure 2b), there was no obvious peak shift or peak broadening observed for C—O—C stretching of Me_2O after dissolving 1 M $LiBF_4$ salt, indicating the low ratio of solvated Me_2O. As a comparison, the DME solvent exhibited an obvious blueshift of C—O—C stretching when 1 M $LiBF_4$ salt was added (Figure S5, Supporting Information). This indicated higher solvated DME represented in the 1 M $LiBF_4$-DME-PC. In addition, the DFT calculations suggested weaker binding between the Me_2O molecule and Li^+ of –1.76 eV than the DME molecule and Li^+ of –2.84 eV (Figure S4, Supporting Information), which was consistent with the Raman observation (Figure 2b). As shown in Figure 2c, the stretching mode of the C=O from PC also varied in different electrolytes, both 1 M $LiBF_4$-DME-PC and 1 M $LiBF_4$-Me_2O-PC showed an obvious blueshift compared with pure PC, where the latter spectrum showed slightly larger shifting, demonstrating the increased coordination between PC and Li^+ inside 1 M $LiBF_4$-Me_2O-PC. Similar observations could also be found that more solvated PC appear in the 1 M $LiBF_4$-Me_2O-PC at the PC ring bending position (Figure S5, Supporting Information). Based on the above observations, the anion-pairing solvation structure of 1 M $LiBF_4$-Me_2O-PC is demonstrated in Figure 2d, which differs from the solvent-coordinated solvation structure of 1 M $LiBF_4$-DME-PC.

MD simulations confirmed the observations from Raman spectroscopy. The simulation boxes contain 1 M $LiBF_4$-DME-PC (Figure 2e) and 1 M $LiBF_4$-Me_2O-PC (Figure 2h). After equilibration, the radial distribution functions (RDFs) for Li^+ in 1 M $LiBF_4$-DME-PC and 1 M $LiBF_4$-Me_2O-PC were computed at both 20 and 0 °C, and the related results are shown in Figure 2f,i. In terms of probability at 20 °C, it was found that DME predominates the solvation shell, whereas BF_4^- anion and PC accounted for lower but comparable percentages (Figure 2f,g), resulting in an average Li coordination environment consisting of 2.3 DME (two oxygen atoms per DME), 0.39 PC, and 0.38 BF_4^-. On the other hand, the most probable coordinating species in 1 M $LiBF_4$-Me_2O-PC is BF_4^-, followed by PC and Me_2O (Figure 2i,j), resulting in an average Li coordination environment consisting of 0.81 Me_2O, 1.1 PC, and 2.4 BF_4^-. It is noteworthy in both cases that although the probability of PC coordination is high, its sparing volumetric composition yields relatively low coordination numbers. In terms of the Me_2O, although the coordination number of Me_2O around 0.81, the relative ratio between solvated and un-solvated Me_2O is extremely low due to the high volumetric ratio of the total Me_2O amount. At 0 °C, it was observed that the solvation structure of the 1 M $LiBF_4$-DME-PC

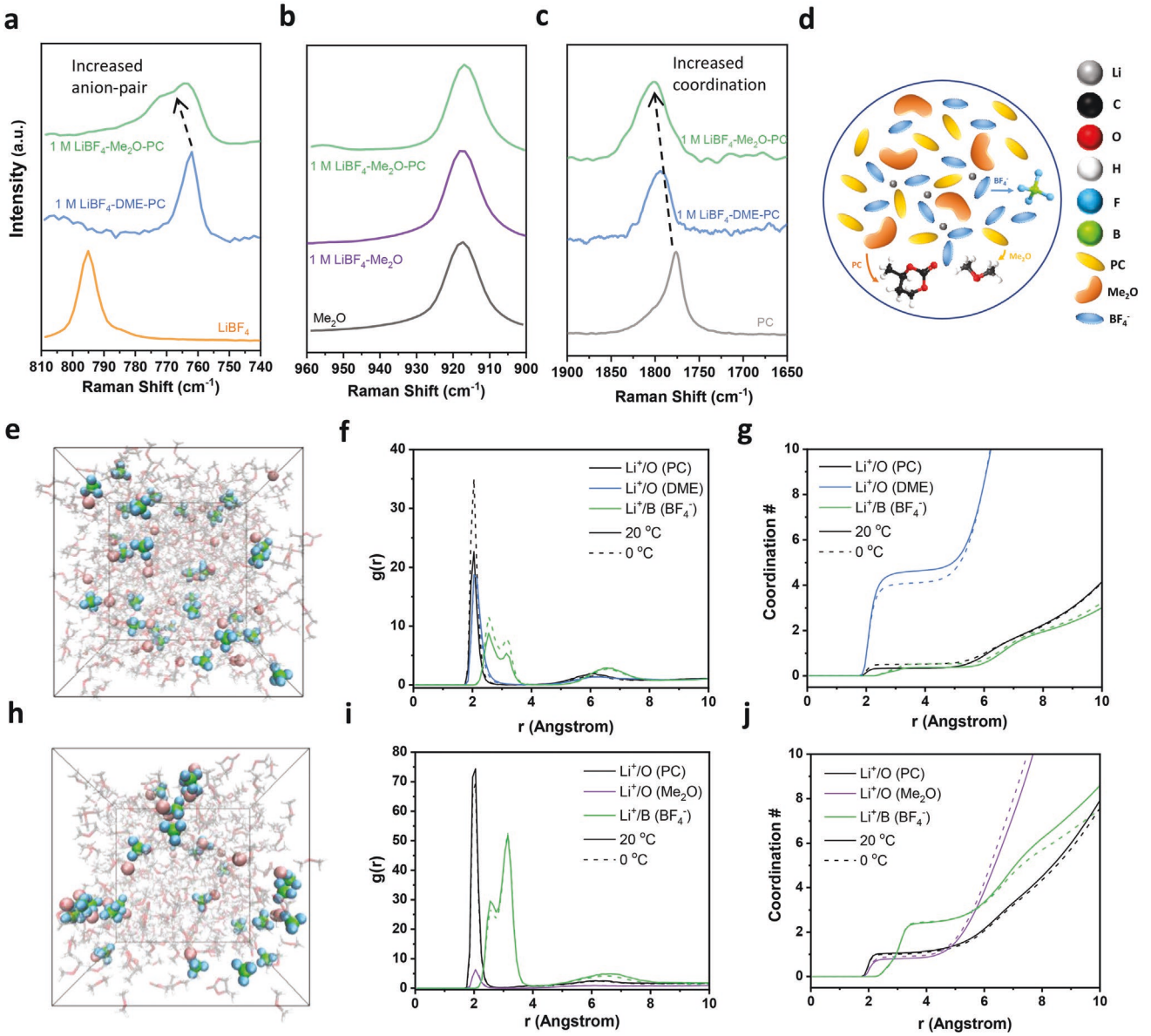

Figure 2. Raman spectra and simulated results of formulated and reference electrolytes. a–c) Raman spectra for $LiBF_4$ salt in different solvents (B—F stretching) (a), Me_2O solvent in different electrolytes (b), and PC solvent in different electrolytes (c). d) Proposed solvation structure of formulated electrolyte. e) Snapshots of the MD simulation cell containing 1 M $LiBF_4$-DME-PC. f,g) Li^+ radial distribution function and coordination number obtained from MD simulations of 1 M $LiBF_4$-DME-PC at both 20 and 0 °C. h) Snapshots of the MD simulation cell containing 1 M $LiBF_4$-Me_2O-PC. i,j) Li^+ radial distribution function and coordination number obtained from MD simulations of 1 M $LiBF_4$-Me_2O-PC at both 20 and 0 °C. In the simulation box, pink represents Li, green represents B, blue represents F, red represents O, gray represents C, and white represents H. Each atom's representative color can also be referred to in the legend of (d).

electrolyte shifts slightly away from DME (2.3 to 2.0) and towards PC (0.39 to 0.52), whereas the 1 M $LiBF_4$-Me_2O-PC showed negligible shift for all molecules (Figure 2i–g), still maintaining anion-pair solvation structure. Importantly, such anion-pairing solvation structure demonstrated improved Li^+ diffusivity of the 1 M $LiBF_4$-Me_2O-PC at 20 and 0 °C compared with that of the 1 M $LiBF_4$-DME-PC (Figure S6, Tables S1 and S2, Supporting Information). Integrated with the increased transport properties, the anion-paired solvation structure has also been proved to significantly benefit the Li^+ de-solvation portion of charge transfer, resulting in facile kinetics and improved low-temperature performance.[14,32,33]

Four operating temperatures (–70, –60, +23, +55 °C) were performed to evaluate the temperature-dependent discharge performance of Li/CF_x cells in the formulated electrolytes. The discharge profiles of the cells with the 1 M $LiBF_4$-Me_2O-PC and 1 M $LiBF_4$-DME-PC electrolytes are shown in **Figure 3**a,b. Under the current density of 10 mA g^{-1}, the two electrolytes delivered similar performances at 23 °C where 1 M $LiBF_4$-DME-PC showed slightly higher discharge capacity and voltage platform

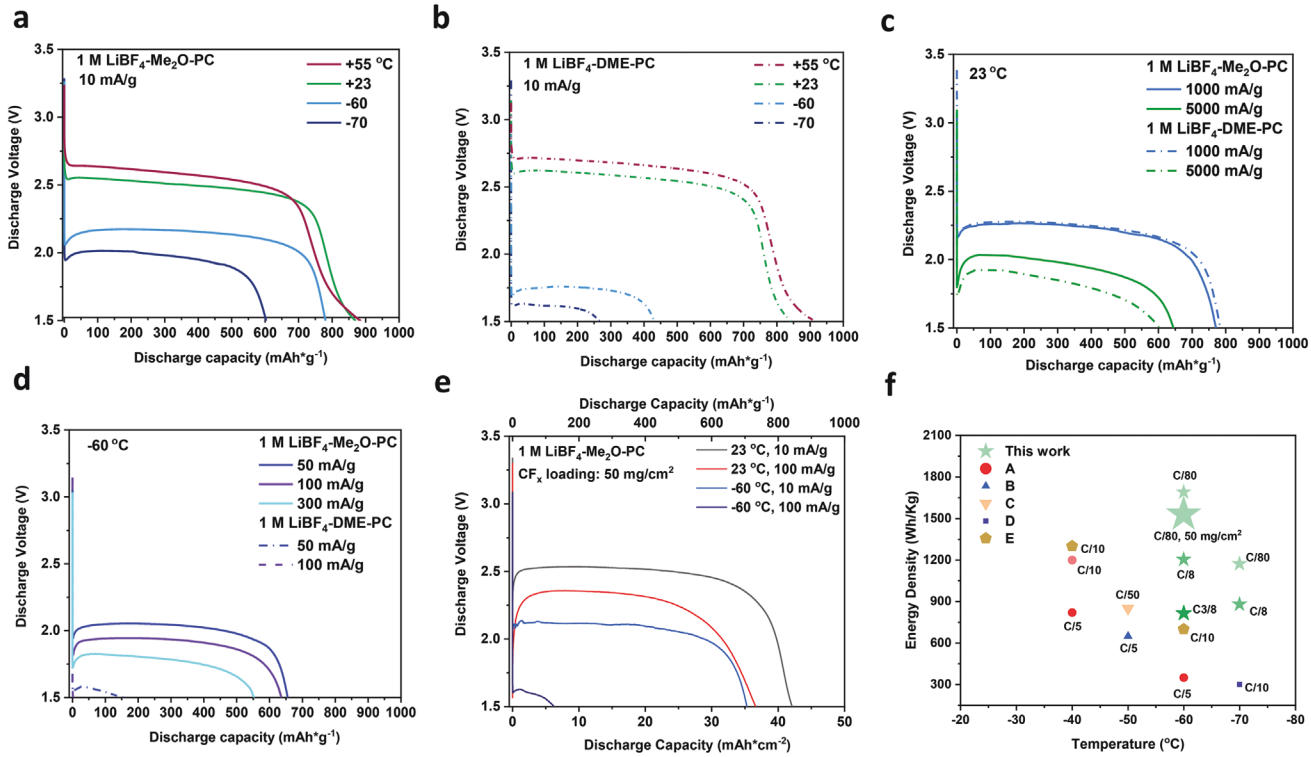

Figure 3. Electrochemical performance of CF_x in different electrolytes. a) Measured electrochemical performance at a wide-temperature range of 1 M $LiBF_4$-Me_2O-PC. b) Measured electrochemical performance at a wide-temperature range of 1 M $LiBF_4$-DME-PC. c) Discharge profiles under different current densities at room temperature. d) Discharge profiles under different current densities at –60 °C. e) Different current density discharge profiles at room temperature and –60 °C using high-loading CF_x. f) Summary of energy density at different temperatures from references (A,[9] B,[34] C,[13] D,[15] E[35]) and this work. The shade of color of each point indicates the current density and the size of each point describes the loading of the electrodes. The lowest reported loading is 1–2 mg cm^{-2} and the highest one is 50 mg cm^{-2}. The 10 mA g^{-1} current density used in this work roughly equals to C/80. It also applied to higher current densities where 100 mA g^{-1} roughly equals to C/8 and 300 mA g^{-1} roughly equals to C3/8.

at 55 °C. However, the 1 M $LiBF_4$-Me_2O-PC electrolyte produced substantially improved performance than 1 M $LiBF_4$-DME-PC, providing 780 mAh g^{-1} and 603 mAh g^{-1} at –60 and –70 °C, respectively, with higher discharge voltage plateaus. In comparison, the 1 M $LiBF_4$-DME-PC electrolyte demonstrated reduced discharge capacities of 431 mAh g^{-1} at –60 °C and 267 mAh g^{-1} at –70 °C, respectively. This difference can be attributed to the higher ionic conductivities of the 1 M $LiBF_4$-Me_2O-PC electrolyte with higher Li^+ diffusivity and a facile de-solvation process enabled by anion-pair solvation structure, which further gives rise to the utilization of CF_x at such low temperatures, as confirmed by the more prominent LiF peaks from X-ray diffraction (XRD) of the discharged CF_x (Figure S7, Supporting Information). Interestingly, the cell employing 1 M $LiBF_4$-Me_2O delivered 708 mAh g^{-1} capacity at –60 °C (Figure S8, Supporting Information), which was lower than the cell using the 1 M $LiBF_4$-Me_2O-PC, but still outperformed both cells discharged in the 1 M $LiBF_4$-DME and 1 M $LiBF_4$-DME-PC, indicating Me_2O is more crucial than PC for the low-*T* performance.

To further evaluate the rate performance, Li/CF_x cells were discharged at increased current densities of 1000 and 5000 mA g^{-1} at room temperature. As shown in Figure 3c, the two electrolytes delivered similar capacities at a current density of 1000 mA g^{-1}. However, under 5000 mA g^{-1}, the 1 M $LiBF_4$-Me_2O-PC demonstrated a higher discharge capacity of 645 mAh g^{-1} when compared to 603 mAh g^{-1} in the 1 M $LiBF_4$-DME-PC. The electrolyte performance at reduced temperatures was also evaluated under increased current densities, as shown in Figure 3d for –60 °C and Figure S9, Supporting Information, for –70 °C. At –60 °C, the 1 M $LiBF_4$-Me_2O-PC retained 63.6% of the CF_x theoretical capacity at a high current density of 300 mA g^{-1} while the 1 M $LiBF_4$-DME-PC failed to discharge at 100 mA g^{-1}. At –70 °C, the 1 M $LiBF_4$-Me_2O-PC electrolyte again demonstrated improved performance against the reference electrolyte which failed to discharge at 100 mA g^{-1}. When using 50 mg cm^{-2} CF_x with 409 µm thickness (Figure S10, Supporting Information), the 1 M $LiBF_4$-Me_2O-PC can discharge at 100 mA g^{-1} with a higher voltage drop (down to 1.57 V) at room temperature (Figure 3e). When the cells were exposed to –60 °C, the cell using 1 M $LiBF_4$-Me_2O-PC maintained 35.3 mAh cm^{-2} capacity (706 mAh g^{-1}) at such extreme conditions (Figure 3e). By contrast, the 1 M $LiBF_4$-DME-PC delivered 855 mAh g^{-1} capacity at room temperature but almost no capacity at –60 °C even with predischarge step (Figure S11, Supporting Information). Even under 100 mA g^{-1} current density at –60 °C, the cell using 1 M $LiBF_4$-Me_2O-PC still delivered 203 mAh g^{-1} capacity with predischarge condition (Figure S12, Supporting Information). In conclusion, the 1 M $LiBF_4$-Me_2O-PC enabled Li/CF_x cells with high energy density at ultralow temperatures when compared with other reported electrolytes, further reinforcing its

promise to enable next-generation primary batteries in extreme environments (Figure 3f, Table S3, Supporting Information).

To comprehend the outstanding performance delivered by 1 M $LiBF_4$-Me_2O-PC, we performed electrochemical impedance spectroscopy (EIS) to monitor the overall impedance during the different depths of discharge in both electrolytes. As shown in Figure S13 and Figure S14, Supporting Information, the EIS spectra were fitted following graphite/electrolyte interface model.[36] The bulk resistance (R_b) of solvated Li^+ in 1 M $LiBF_4$-Me_2O-PC remained stable over different depth of discharge states and was consistently lower than the 1 M $LiBF_4$-DME-PC (Figure S14, Supporting Information), which aligned with the ionic conductivity results in Figure 1. In terms of the charge-transfer impedance (R_{ct}), which represents the breakup of the solvation shell of Li^+, 1 M $LiBF_4$-Me_2O-PC had an R_{ct} 2–4 times lower than that of 1 M $LiBF_4$-DME-PC before reaching the 20 h discharge, where the turning points occured between the 10 and 20 h discharge state. After the 20 h discharge, the charge-transfer resistance was significantly reduced in the 1 M $LiBF_4$-DME-PC but still higher than its counterpart. During the entire discharge, 1 M $LiBF_4$-Me_2O-PC possessed lower interfacial impedance (R_{int}), which indicated lower Li^+ diffusion barriers through the SEI/CEI. It is well-known that the interface plays an important role in the charge-transfer kinetics, which is correlated to the de-solvation process of the electrolytes near the interface, the diffusion through CEI, and the chemistry and structure of CEI.[37] Considering the complexity of de-convoluting each step, X-ray photoelectron spectroscopy (XPS) was performed on the 10 h discharged CF_x at −60 °C to investigate if the chemical composition of CEI determines the charge-transfer impedance difference, and the data are shown in **Figure 4**a–f. Given that both samples were stopped at the same discharge capacity, the formed LiF and carbon should be the same in quantity. Based on the global survey of discharged CF_x, similar F, B, and O atomic concentrations were observed over different etching times (Figure 4b,c). This indicated the similarity of interfacial chemistry in both electrolytes. We further examined the fine spectra of different elements. The C 1s from the pristine CF_x electrode showed the characteristic structure of CF_x materials, mainly containing C—C, C—F, and C—F_2 bonds (Figure 4d). After discharge, C—F/C—F_2 peaks decreased drastically, indicating the electrochemical reaction. Apart from that, CEI information was depicted by O 1s signal because the source of extra oxygen came from the electrolyte decomposition. After 10 h discharge, a new C=O appeared in both C 1s and O 1s spectra with a relatively weak intensity over different etching conditions, implying a thin CEI formed in both electrolytes. Interestingly, there is no obvious

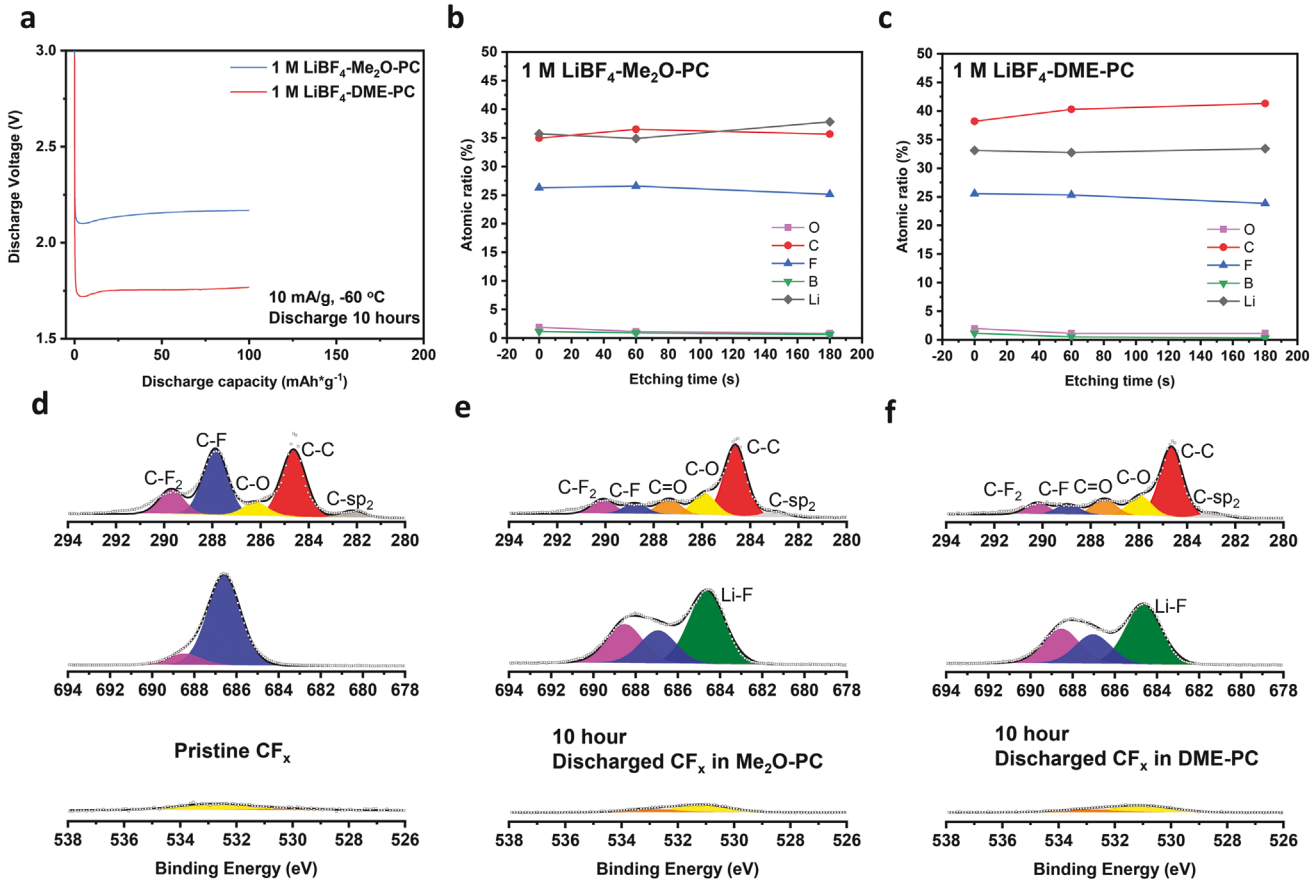

Figure 4. Global and local XPS analysis of the CF_x at different states. a) Voltage profiles of 10 h discharged CF_x in both electrolytes. b,c) Summary of atomic concentration of CF_x discharged in 1 M $LiBF_4$-Me_2O-PC (b) and 1 M $LiBF_4$-DME-PC (c). d) Local survey of pristine CF_x. e) Local survey of 10 h discharged CF_x in 1 M $LiBF_4$-Me_2O-PC. f) Local survey of 10 h discharged CF_x in 1 M $LiBF_4$-DME-PC. As for the XPS spectra, those represent C 1s spectra, F 1s spectra, and O 1s spectra from top to bottom view.

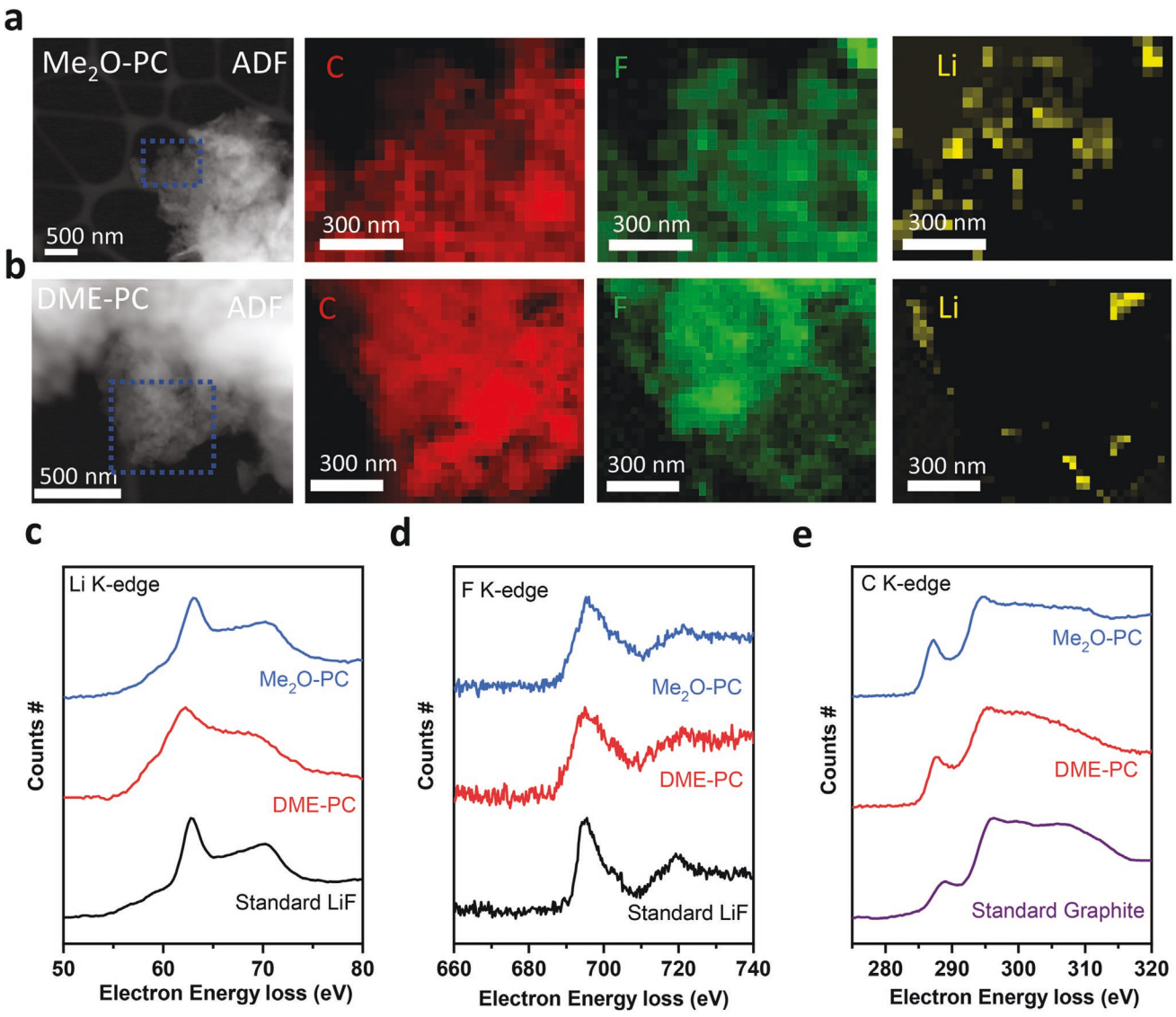

Figure 5. STEM–EELS, HRTEM, and SAED of the 10 h discharged CF_x at –60 °C. a,b) STEM image and EELS mappings of discharged CF_x in 1 M $LiBF_4$-Me_2O-PC (a) and 1 M $LiBF_4$-DME-PC (b). c–e) EELS spectra of Li K-edge (c), F K-edge (d), and C K-edge (e).

difference between both electrolytes in all XPS spectra, in addition to the more predominated C and F 1s signal (Figure 4e,f). When fully discharged to 1.5 V, higher Li—F, less carbonyl group, and C—C signal were observed in CF_x discharged in 1 M $LiBF_4$-Me_2O-PC due to higher CF_x utilization (Figure S15, Supporting Information). Based on the above analysis, we can conclude that CEI chemistry exerts nonobvious influence on low-*T* performance.

To understand the local CF_x structure change during low-*T* discharge, scanning transmission electron microscopy–electron energy loss spectroscopy (STEM–EELS), high-resolution transmission electron microscopy (HRTEM), and selected-area electron diffraction (SAED) were performed on CF_x samples discharged at –60 °C in different electrolytes under 10 mA g^{-1} (**Figure 5**a–e, Figures S16–S18, Supporting Information). Based on the STEM images and elemental mappings of discharged CF_x, a greater prevalence of Li was observed in 10 h discharged CF_x in the 1 M $LiBF_4$-Me_2O-PC compared to the 1 M $LiBF_4$-DME-PC at selected areas (Figure 5a,b). Both samples demonstrated the C and F elements with the new appearance of Li elements, where the Li distribution was more homogeneous in the discharged CF_x in 1 M $LiBF_4$-Me_2O-PC. Coupled with EELS spectra (Figure 5c–e), both samples showed Li—F features as standard LiF sample, indicating the breaking of C—F bond and the formation of Li—F and graphitic carbon after 10 h discharge. The inhomogeneity of LiF formation and scattered distribution of unreacted CF_x from the CF_x discharged in 1 M $LiBF_4$-DME-PC confirmed the sluggish transport/de-solvation properties of the 1 M $LiBF_4$-DME-PC electrolyte, which, in contrast, highlighted the superior performance enabled by the 1 M $LiBF_4$-Me_2O-PC with the homogeneous distribution of the discharged products. The fully discharged CF_x were also evaluated, and the results were consistent with the observations from the 10 h discharged samples (Figures S17 and S18, Supporting

Information). Considering the significantly reduced interfacial resistance obtained from the 1 M $LiBF_4$-Me_2O-PC electrolyte (Figure S13, Supporting Information) for Li/CF_x cell, the LGE should benefit the Li-metal side as reported before,[27] where Me_2O-based LGE demonstrated improved SEI structure compared with DME-based liquid electrolyte for lithium-metal cycling at both room temperature and reduced temperature. Integrated with the above analysis, we can conclude that the structure of discharge products (LiF and graphitic carbon) appears similarly in both electrolytes and also places unimportant influences on low-*T* performance. Instead, bulk ionic transport and Li^+ de-solvation are more critical factors affecting the utilization of CF_x and the distribution of discharge products.

3. Conclusion

1 M $LiBF_4$-Me_2O-PC electrolyte has been well-formulated to improve the temperature-dependent and rate-dependent performance of Li/CF_x primary battery. The optimized electrolyte demonstrated >3.5 mS cm^{-1} ionic conductivity through a wide temperature range of –70 to 60 °C. Raman, MD, and DFT simulations suggested the formulated electrolyte features anion-pairing solvation of which the predominating Me_2O molecules have a weak affinity with Li^+, facilitating the rate capability and low-temperature operation by affecting the de-solvation process while maintaining decent transport. Benefitting from the fast kinetics of the de-solvation and bulk transport, the optimized electrolyte enables high utilization of CF_x, demonstrating excellent rate performance at both room temperature and –60 °C and high energy over an extended operating temperature window (–70 to +55 °C). XPS and STEM–EELS revealed that the CEI chemistry had little impact on the low-*T* performance, highlighting the importance of electrolyte de-solvation and bulk transfer features. This work provides a route to enable high power and high energy density Li/CF_x batteries operated in the extreme low-*T* environment, which may enlighten advanced primary battery designs with high energy and power in the future.

4. Experimental Section

Materials: Dimethyl ether (99%) was obtained from Sigma-Aldrich. The salts lithium bis(fluorosulfonyl)imide (99.9%) and lithium bis(trifluoromethane)sulfonimide (99.9%) were purchased from BASF and lithium tetrafluoroborate was purchased from Sigma-Aldrich. 1,2-Dimethoxyethane (99.5%) and propylene carbonate were purchased from Sigma-Aldrich and stored over molecular sieves for more than two days before formulating the electrolytes. The CF_x powders were purchased from ACS material (GT1FS012). The CF_x electrodes were made with an 8:1:1 ratio between active materials: PVDF:C65 and cast on Al foils. All cast electrodes were dried at 80 °C overnight before use. The CF_x electrode loading was approximately 4.3 mg cm^{-2}.

Fabrication of 50 mg cm^{-2} CF_x cathodes was accomplished by forming and rolling a dough. First carbon black (Super-P) was mixed with a commercial carbon fluoride (Advanced Research Chemicals, ARC-5-R-175) in a 5:95 wt% ratio by using a mortar and pestle. Once thoroughly mixed, 5.6 wt% Teflon (60 wt% suspension in H_2O, Sigma-Aldrich) was added dropwise to the powder and mixing via mortar and pestle continued. With the addition of binder, the powder began to agglomerate, although not all powder adhered into one mass. To ensure a proper dough another 6.5 wt% of Teflon (wt% including previous Teflon addition) was mixed in with mortar and pestle. A small amount of isopropyl alcohol was used to wet the mixture and facilitate the spread of Teflon among the carbon and CF_x powders. After approximately 10 min of hand mixing after the second Teflon addition, a dough formed that was free-standing and did not shed powder. The dough was then rolled on a glass slab with a glass rolling pin to a thickness of ≈0.5 mm and then dried at 80 °C for 12 h.

Electrochemical Measurements: Ionic conductivity of different electrolytes was performed in custom-fabricated pressurized stainless-steel cells with polished stainless-steel (SS 316L) as both electrodes. OAKTON standard conductivity solutions (0.447 to 80 mS cm^{-1}) were utilized to frequently calibrate the cell constant for the cells.

Electrochemical impedance spectroscopy was collected by a Biologic SAS (SP-200) system and the spectra were then fitted using ZView 4 software.

Battery discharging tests were performed using an Arbin battery test station (BT2043) from Arbin Instruments in custom-designed pressurized stainless-steel cells. Li metal (FMC Lithium, 1 mm thickness, 3/8-inch diameter), separators, and CF_x electrodes were sandwiched, where Li metal serves as counter electrode and the CF_x serves as working electrode. A three-layer 25 µm porous PP/PE/PP membrane (Celgard 2325) was used for all the electrochemical tests. The electrolyte amount was flooded (>50 g Ah^{-1}) for all electrolytes mentioned in this work.

For Li/CF_x discharge tests in different temperatures, the cells were soaked at the testing temperature in a temperature chamber (Espec) for at least 2 h before discharge. All room temperature discharge tests were performed without controlling the temperature. The pre-discharge of Li/CF_x with 50 mg cm^{-2} cathodes was performed at room temperature for 2 h discharge using 10 mA g^{-1}.

Material Characterization: The XRD measurements were done by a Bruker APEX II Ultra diffractometer with Mo Kα (λ = 0.71073 Å) radiations to check the crystal structures. The samples were prepared by scratching the cathode electrode and filling the capillary tubes inside an Ar-filled glovebox. All the cathode samples were not washed before these measurements.

Superlow-dose TEM/EELS techniques were developed for characterizing CF_x structures. The discharged CF_x cathodes were rinsed with DME to remove residual salt and dried at 80 °C under vacuum on a hotplate prior to analysis. The cathode powders were scratched from electrodes and put on a Cu TEM grid for all measurements. HRTEM samples were transferred into the TEM (ThermoFisher Talos 200X TEM operated at 200 kV), which was equipped with a CETA camera and low-dose system. The HRTEM images in panel D&F were acquired with an electron dose rate of ≈200 e $Å^{-2}$ s^{-1} for ≈1s. The STEM (EELS Mapping) samples were also transferred into the ThermoFisher Talos 200X TEM. The TALOS microscope was equipped with a high-resolution Gatan imaging filter (Gatan Continuum 1069) for EELS mapping. The probe current utilized for EELS maps on the TALOS was approximately 140 pA.

Raman spectra of liquefied gas electrolytes were carried on Renishaw inVia confocal Raman microscope with an excitation wavelength of 532 nm. All spectra were calibrated with Si (520 nm) and analyzed by Wire 3.4 software developed by Renishaw Ltd. The Raman spectra measurements of Me_2O-based electrolytes were performed in a custom-built pressurized cell.[30]

XPS was performed using a Kratos AXIS Supra DLD XPS with monochromatized Al Kα radiation (λ = 0.83 nm and $h\upsilon$ = 1486.7 eV) under a base pressure <10^{-8} Pa. To avoid moisture and air exposure, samples were transferred to the XPS chamber directly from a glovebox via air-tight transfer. All spectra were calibrated with hydrocarbon C–H C 1s (284.6 eV) and analyzed by CasaXPS software. To remove residual salt on the surface, all samples were rinsed with DME and dried in glovebox antechamber before analysis. The etching condition was set as an Ar1000+ cluster at 5 keV. The etching times were 60 and 180 s.

Computational Analysis: Classical, fixed-charge molecular dynamics (MD) simulations were performed in LAMMPS using the General Amber forcefield for solvents and Li^+ with the anion described with the potentials of Doherty et al.[38] Liquid simulation boxes were constructed from random, amorphous distributions of the molecules, with compositions corresponding to the volume ratios and salt concentrations described above. In all cases, the charges of the Li^+ and FSI^- molecules were scaled to the optical dielectric of the solvents present in the system as employed by Park et al.,[39] which was 0.72 for DME/PC and 0.76 for Me_2O/PC. Periodic boundary conditions were applied in all directions.

For each system, the step size for all simulations was 1 fs. First, an initial energy minimization at 0 K (energy and force tolerances of 10^{-4}) was performed, after which the system was slowly heated from 0 to 298 K at constant volume over 0.01 ns using a Langevin thermostat, with a damping parameter of 100 ps. The system was then subjected to 5 cycles of quench-annealing dynamics in an effort to eliminate the existence of metastable solvation states, where the temperature was cycled between 298 and 894 K at a ramp period of 0.025 ns followed by 0.1 ns of dynamics at either temperature extreme with a total of 1.25 ns for all 5 cycles. After annealing, the system was equilibrated in the constant temperature and constant pressure (NpT ensemble) for 1.5 ns. The applied pressure was 1 atm for DME/PC and 4.83 atm for Me_2O/PC, which was the experimental electrolyte pressure measured with Honeywell FP5000 pressure sensor at room temperature. The stresses in the system were isotropically resolved using the Andersen barostat at a pressure relaxation constant of 1 ps). Finally, 10 ns of constant volume, constant temperature (NVT) production dynamics was performed. Radial distribution functions and solvation snapshots sampled from the MD trajectory were obtained using the Visual Molecular Dynamics (VMD) software.

DFT binding energy calculations were performed using the Q-Chem 5.1 package. A geometry optimization step at the B3LYP//6-31+G(d,p) level of theory was followed by single point energy calculations at the B3LYP//6-311++G** level of theory. Solvent binding energies were calculated as:

$$\Delta E = E_{Li^+ + solvent} - \left(E_{Li^+} + E_{Solvent}\right) \quad (1)$$

Supporting Information

Supporting Information is available from the Wiley Online Library or from the author.

Acknowledgements

This work was supported partially by the Laboratory Directed Research and Development program (Project 218253) at Sandia National Laboratories, a multi-mission laboratory managed and operated by National Technology and Engineering Solutions of Sandia, LLC., a wholly owned subsidiary of Honeywell International, Inc., for the U.S. Department of Energy's National Nuclear Security Administration under contract DE-NA-0003525. The views expressed herein do not necessarily represent the views of the U.S. Department of Energy or the United States Government. This work was supported partially by an Early Career Faculty grant from NASA's Space Technology Research Grants Program (ECF 80NSSC18K1512) to Z.C. The SEM was performed in part at the San Diego Nanotechnology Infrastructure (SDNI) of UCSD, a member of the National Nanotechnology Coordinated Infrastructure, which was supported by the National Science Foundation (Grant ECCS-1542148). Y.Y. thanks Ich C. Tran for their help regarding XPS experiments performed at the University of California Irvine Materials Research Institute (IMRI) using instrumentation funded in part by the National Science Foundation Major Research Instrumentation Program (grant CHE-1338173). The authors acknowledge the use of Raman instrumentation supported by NSF through the UC San Diego Materials Research Science and Engineering Center (UCSD MRSEC), grant # DMR-2011924. The authors would like to acknowledge the UCSD Crystallography Facility.

Conflict of Interest

The authors declare no conflict of interest.

Author Contributions

Y.Y., Z.C., and Y.S.M. conceived the original idea. Y.Y. and W.L. designed the experimental plan. Y.Y. and A.L. carried out the experiments. J.H. developed force field and conducted the MD simulations. G.R. and G.C. assisted with control experiments. B.S. performed the XRD characterization. Y.Y. and W.L. performed the XPS characterization and analysis. B.H. and Y.Y. performed the STEM–EELS characterization and analysis. N.B.S., T.N.L., and K.L.H. developed and fabricated high-loading CF_x electrodes. Y.Y., J.H., and W.L. prepared the manuscript with input from all co-authors. All authors have given approval to the final version of the manuscript.

Data Availability Statement

The data that support the findings of this study are available from the corresponding author upon reasonable request.

Keywords

anion-pairing and fast-transport electrolytes, electrode interfaces, lithium-fluorinated carbon primary batteries, thick loading electrodes, ultralow temperature and high current operation

Received: August 30, 2022
Revised: October 10, 2022
Published online:

[1] J.-P. Jones, S. C. Jones, F. C. Krause, J. Pasalic, M. C. Smart, R. V. Bugga, E. J. Brandon, W. C. West, *J. Electrochem. Soc.* **2017**, *164*, A3109.
[2] F. C. Krause, J.-P. Jones, S. C. Jones, J. Pasalic, K. J. Billings, W. C. West, M. C. Smart, R. V. Bugga, E. J. Brandon, M. Destephen, *J. Electrochem. Soc.* **2018**, *165*, A2312.
[3] Q. Zhang, K. J. Takeuchi, E. S. Takeuchi, A. C. Marschilok, *Phys. Chem. Chem. Phys.* **2015**, *17*, 22504.
[4] J. Wolfenstine, D. Foster, W. Behl, S. Gilman, Army Research Lab Adelphi Md Sensors and Electron Devices Directorate, **1998**.
[5] H. D. Lim, H. Park, H. Kim, J. Kim, B. Lee, Y. Bae, H. Gwon, K. Kang, *Angew. Chem., Int. Ed.* **2015**, *54*, 9663.
[6] A. Hills, N. Hampson, *J. Power Sources* **1988**, *24*, 253.
[7] G. Nagasubramanian, *ECS Trans.* **2008**, *11*, 19.
[8] D. C. Bock, A. C. Marschilok, K. J. Takeuchi, E. S. Takeuchi, *Electrochim. Acta* **2012**, *84*, 155.
[9] J. Whitacre, W. West, M. Smart, R. Yazami, G. S. Prakash, A. Hamwi, B. Ratnakumar, *Electrochem. Solid-State Lett.* **2007**, *10*, A166.
[10] B. Sayahpour, H. Hirsh, S. Bai, N. B. Schorr, T. N. Lambert, M. Mayer, W. Bao, D. Cheng, M. Zhang, K. Leung, K. L. Harrison, W. Li, Y. S. Meng, *Adv. Energy Mater.* **2022**, *12*, 2103196.
[11] K. Leung, N. B. Schorr, M. Mayer, T. N. Lambert, Y. S. Meng, K. L. Harrison, *Chem. Mater.* **2021**, *33*, 1760.

[12] J. Whitacre, R. Yazami, A. Hamwi, M. C. Smart, W. Bennett, G. S. Prakash, T. Miller, R. Bugga, *J. Power Sources* **2006**, *160*, 577.
[13] S. S. Zhang, D. Foster, J. Read, *J. Power Sources* **2009**, *188*, 532.
[14] Q. Li, D. Lu, J. Zheng, S. Jiao, L. Luo, C.-M. Wang, K. Xu, J.-G. Zhang, W. Xu, *ACS Appl. Mater. Interfaces* **2017**, *9*, 42761.
[15] Z. Fang, Y. Yang, T. Zheng, N. Wang, C. Wang, X. Dong, Y. Wang, Y. Xia, *Energy Storage Mater.* **2021**, *42*, 477.
[16] J. Holoubek, H. Liu, Z. Wu, Y. Yin, X. Xing, G. Cai, S. Yu, H. Zhou, T. A. Pascal, Z. Chen, *Nat. Energy* **2021**, *6*, 303.
[17] J. Holoubek, K. Kim, Y. Yin, Z. Wu, H. Liu, M. Li, A. Chen, H. Gao, G. Cai, T. A. Pascal, *Energy Environ. Sci.* **2022**, *15*, 1647.
[18] J. Zheng, P. Yan, D. Mei, M. H. Engelhard, S. S. Cartmell, B. J. Polzin, C. Wang, J. G. Zhang, W. Xu, *Adv. Energy Mater.* **2016**, *6*, 1502151.
[19] X. Cao, H. Jia, W. Xu, J.-G. Zhang, *J. Electrochem. Soc.* **2021**, *168*, 010522.
[20] J. Holoubek, A. Baskin, J. W. Lawson, H. Khemchandani, T. A. Pascal, P. Liu, Z. Chen, *J. Phys. Chem. Lett.* **2022**, *13*, 4426.
[21] A. C. Thenuwara, P. P. Shetty, N. Kondekar, S. E. Sandoval, K. Cavallaro, R. May, C.-T. Yang, L. E. Marbella, Y. Qi, M. T. McDowell, *ACS Energy Lett.* **2020**, *5*, 2411.
[22] C. S. Rustomji, Y. Yang, T. K. Kim, J. Mac, Y. J. Kim, E. Caldwell, H. Chung, Y. S. Meng, *Science* **2017**, *356*, eaal4263.
[23] G. Cai, Y. Yin, D. Xia, A. A. Chen, J. Holoubek, J. Scharf, Y. Yang, K. H. Koh, M. Li, D. M. Davies, *Nat. Commun.* **2021**, *12*, 3395.
[24] Y. Yang, D. M. Davies, Y. Yin, O. Borodin, J. Z. Lee, C. Fang, M. Olguin, Y. Zhang, E. S. Sablina, X. Wang, *Joule* **2019**, *3*, 1986.
[25] Y. Yang, Y. Yin, D. M. Davies, M. Zhang, M. Mayer, Y. Zhang, E. S. Sablina, S. Wang, J. Z. Lee, O. Borodin, *Energy Environ. Sci.* **2020**, *13*, 2209.
[26] E. P. Hunter, S. G. Lias, *J. Phys. Chem. Ref. Data* **1998**, *27*, 413.
[27] Y. Yin, Y. Yang, D. Cheng, M. Mayer, J. Holoubek, W. Li, G. Raghavendran, A. Liu, B. Lu, D. M. Davies, *Nat. Energy* **2022**, *7*, 548.
[28] R. Jow, S. S. Zhang, K. Xu, J. Allen, *ECS Trans.* **2007**, *3*, 51.
[29] K. Xu, *Chem. Rev.* **2004**, *104*, 4303.
[30] D. M. Davies, Y. Yang, E. S. Sablina, Y. Yin, M. Mayer, Y. Zhang, M. Olguin, J. Z. Lee, B. Lu, D. Damien, *J. Power Sources* **2021**, *493*, 229668.
[31] T. Doi, Y. Shimizu, M. Hashinokuchi, M. Inaba, *J. Electrochem. Soc.* **2017**, *164*, A6412.
[32] B. Huang, K. H. Myint, Y. Wang, Y. Zhang, R. R. Rao, J. Sun, S. Muy, Y. Katayama, J. Corchado Garcia, D. Fraggedakis, *J. Phys. Chem. C* **2021**, *125*, 4397.
[33] A. Baskin, J. W. Lawson, D. Prendergast, *J. Phys. Chem. Lett.* **2021**, *12*, 4347.
[34] G. Nagasubramanian, M. Rodriguez, *J. Power Sources* **2007**, *170*, 179.
[35] W. Xue, T. Qin, Q. Li, M. Zan, X. Yu, H. Li, *Energy Storage Mater.* **2022**, *50*, 598.
[36] K. Xu, *J. Electrochem. Soc.* **2007**, *154*, A162.
[37] Z. Zhang, J. Yang, W. Huang, H. Wang, W. Zhou, Y. Li, Y. Li, J. Xu, W. Huang, W. Chiu, *Matter* **2021**, *4*, 302.
[38] B. Doherty, X. Zhong, S. Gathiaka, B. Li, O. Acevedo, *J. Chem. Theory Comput.* **2017**, *13*, 6131.
[39] C. Park, M. Kanduč, R. Chudoba, A. Ronneburg, S. Risse, M. Ballauff, J. Dzubiella, *J. Power Sources* **2018**, *373*, 70.